Source characterization of full-scale tactical jet noise from phased-array measurements

Blaine M. Harker, Kent L. Gee, Tracianne B. Neilsen, Alan T. Wall, and Michael M. James

Citation: The Journal of the Acoustical Society of America **146**, 665 (2019); doi: 10.1121/1.5118239
View online: https://doi.org/10.1121/1.5118239
View Table of Contents: https://asa.scitation.org/toc/jas/146/1
Published by the Acoustical Society of America

Source characterization of full-scale tactical jet noise from phased-array measurements

Blaine M. Harker,[a] Kent L. Gee, and Tracianne B. Neilsen
Department of Physics and Astronomy, Brigham Young University, Provo, Utah 84602, USA

Alan T. Wall
Battlespace Acoustics Branch, Air Force Research Laboratory, Wright-Patterson AFB, Ohio 45433, USA

Michael M. James
Blue Ridge Research and Consulting, LLC, Asheville, North Carolina 28801, USA

(Received 22 June 2018; revised 24 June 2019; accepted 29 June 2019; published online 31 July 2019)

Application of phased-array algorithms to acoustic measurements in the vicinity of a high-performance military aircraft yields equivalent source reconstructions over a range of engine conditions. Beamforming techniques for aeroacoustics applications have undergone significant advances over the past decade to account for difficulties that arise when traditional methods are applied to distributed sources such as those found in jet noise. The hybrid method, an inverse method approached via beamforming, is applied to jet noise measured along a 50 element, 30 m linear array to obtain equivalent source distributions. The source distribution extent decreases with increasing frequency or with a decrease in engine condition. A source coherence analysis along the axial dimension of the jet plume reveals that the source coherence lengths scale inversely with increasing engine condition. In addition, a method for extending the array bandwidth to frequencies beyond the spatial Nyquist frequency limit is also implemented. A directivity analysis of the beamforming results reveals that sources near the nozzle radiate to the sideline from a relatively stationary point irrespective of frequency, while the noise source origin of downstream radiating noise varies significantly with frequency. https://doi.org/10.1121/1.5118239

[PBB] Pages: 665–680

I. INTRODUCTION

Acoustic imaging techniques use phased-arrays to provide a unique perspective to jet-noise-source characterizations. While computational fluid dynamics (CFD)[1,2] and particle image velocimetry (PIV)[3] studies are useful to model or measure the turbulence, difficulties exist in attempting to relate the flow properties to the corresponding acoustic radiation.[4] Phased-array techniques, e.g., beamforming, instead rely on the acoustic radiation to estimate the corresponding sources and thereby complement flow-field investigations. Standard beamforming can localize the jet noise sources, while more generalized methods—which have ties to both beamforming and source identification methods[5,6]—can estimate both the levels and coherence properties of the resulting source distributions. Application of generalized beamforming methods require additional considerations due to the directive, extended, and partially correlated sources of the jet noise. Full-scale, tactical aircraft noise characterization is desirable due to the myriad of difficulties of scaling up laboratory-based models to real-world fighter jet engines. In this paper, a hybrid method is applied to measurements of jet noise from a tactical aircraft along a linear uniform array. The results are used to estimate the source distribution properties, including the coherence characteristics.

A. Traditional beamforming and jet noise

Standard data-independent beamforming techniques have had some success in estimating jet noise source properties.[7–9] Phased-array methods are particularly useful in full-scale applications, where the direct measurement of flow parameters is difficult due to the heated, turbulent nature of the flow field.[9–11] Phased arrays capture the radiation for full-scale jets, which consists primarily of contributions from large- and fine-scale turbulent mixing noise[12] as well as other mechanisms such as broadband shock-associated noise.[13] While some studies have used more conventional beamforming techniques to acoustically image these phenomena,[14] many have expanded upon the conventional beamforming assumptions (i.e., incoherent monopoles or well-separated coherent sources).[5] Venkatesh *et al.*[7] proposed an integration beamforming method to account for the distributed nature of the source but without explicitly incorporating source correlation. Schlinker *et al.*[9] applied this method using phased-array measurements from a ground-based array of a supersonic tactical engine. The 30-element 3.9 m array measurements, positioned in the maximum radiation region, were input into the beamforming method and produced relatively consistent source estimates across frequency in terms of peak location and extent. However, the limited aperture prevented a more detailed perspective. Brusniak *et al.*[10] produced an extensive dataset with multiple arrays—including a polar array, multiple parallel linear arrays, and a multi-arm spiral—to measure jet noise sources

[a]Electronic mail: blaineharker@gmail.com

at the nozzle exit and downstream of a full-scale commercial grade engine. The linear arrays spanned about 27 m in length and contained 181 microphones for a dense spacing near the jet mixing noise. Using conventional beamforming, they found that, while the polar array was useful for limited low-frequency jet noise source estimates and for characterizing the core and fan noise, the linear array was most appropriate to estimate the turbulent mixing noise properties of full-scale, tactical aircraft engine. Measurements from the two arrays were compared for consistency, and conventional beamforming results along the jet centerline were obtained. They found that the use of 15 small subarrays and extreme array steering angles potentially produced erroneous results when estimating source component characteristics. However, because traditional beamforming methods process each acoustic source independently, the assumptions may also have impaired the source characterizations.

Much has been done in beamforming jet noise studies using more traditional beamforming methods, but the investigations are limited by the standard beamforming assumption that the sources may be processed independently, i.e., that the sources consist of a distribution of incoherent monopoles and/or sufficiently separated coherent monopoles.[5] Because jet noise sources contain multiple components that are extended, superimposed, and partially correlated in nature,[3,15,16] standard beamforming results can produce misleading source locations and levels.[2,17] More advanced beamforming methods [e.g., the hybrid method (HM)[18]] extend capabilities commonly found in identification methods to solve the acoustic sources together as a system.

In addition to the choice of beamforming method, the measurement array geometry requires consideration. While far-field measurements can be used as inputs to phased-array methods, the results are significantly improved when the array spans the source distribution and is placed in the geometric near field.[17,19] For instance, the source resolution (i.e., the Rayleigh criterion[17]) approximately scales with the measurement distance and as the inverse of the array length.[20] In many circumstances, linear arrays are used in lab-scale[14] and full-scale environments,[21] both to span the jet noise source and to feasibly capture the salient features of the jet noise.[9,10,22] In practical considerations, the relatively low element count and the ability to span large jet noise sources make linear arrays convenient for jet noise experiments. A linear uniform array is utilized in this study to measure jet noise from a tactical aircraft, which will be input to a hybrid beamforming method to estimate the source distribution properties.

B. Advanced beamforming in jet noise

More advanced beamforming techniques applied to full-scale jet noise measurements have provided increased capabilities to characterize the acoustic source properties. The aeroacoustics community has developed improved beamforming methods that share many similarities with identification methods[6]—such as near-field acoustical holography (NAH)[23] and Helmholtz equation least squares (HELS)[24]—to solve for acoustic sources as a system instead of independently.[5] Dougherty and Mendoza[11] applied near-field beamforming and deconvolution techniques [i.e., the deconvolution approach for the mapping of acoustic sources (DAMAS)[25] and CLEAN for spatial source coherence (CLEAN-SC)[26]] to engine and jet noise beamforming results using measurements from a 100-ft-radius polar arc array near a Honeywell Tech977 engine. They showed that the deconvolution improves the beamforming results by providing high resolution images of the source levels as well as a reduction in side-lobe levels. Michel and Funke[22] developed the SODIX method (source directivity modeling of the cross-spectral matrix) to model full-scale jet engine noise that can be used to spatially separate the contributions from the radiating sources (e.g., aft fan, core, and jet noise). They used linear array measurements of a full-scale turbofan engine and applied their method to successfully predict the far-field radiation level contributions from each of the components. Fleury and Davy[27] used a combination of linear arrays and a derivative method of DAMAS-C to map the jet noise acoustic sources of a large-scale dual-core cold jet engine. They were able to separate the turbulent mixing noise from nozzle exit noise and shock-associated noise by comparing the properties of the source cross-spectral matrix. In addition, Padois *et al.*[28] tested the HM and briefly compared this with DAMAS and CLEAN-SC on a full-scale aero-engine. When DAMAS was applied in addition to this hybrid method, the iterative deconvolution results converged more quickly and required fewer iterations. The previous full-scale tactical aircraft noise studies have analyzed source level properties, although a limited full-scale source coherence analysis has only recently been performed.[29] Furthermore, an in-depth characterization of the source levels and coherence properties is lacking, particularly for tactical engines. More sophisticated beamforming and identification methods, described in Refs. 2, 5, and 6, can potentially improve the source property estimates, which are useful to better understand additional hypothesized source mechanisms for heated supersonic jets.[30–32]

C. Overview

The focus of this paper is to develop an acoustic-imaging-based equivalent source model containing source characteristics of turbulent mixing noise from an installed tactical aircraft engine by applying a near-field, coherence-based imaging method to the noise measured on a linear microphone array in the mid field of the jet. While similar in many respects to previous correlated source mapping techniques,[33,34] the HM (Ref. 18) was found to outperform many similar advanced beamforming methods in Ref. 35 and is applied here to improve the source localization and to estimate potential coherence across the source distribution. In addition, the unwrapped-phase array interpolation (UPAINT) method—recently developed for interpolating levels and phase information along the measurement array—is applied to suppress adverse grating lobe effects and extend the usable frequency bandwidth beyond the spatial Nyquist frequency.[36,37] The HM-based source is used to compare the predicted sound pressure levels with those measured at various points in the mid field of the jet.

Further analyses of the HM results provide insight into the source levels and coherence properties of the full-scale,

tactical aircraft engine noise. The results consist of frequency-dependent, complex, source cross-spectral matrices (SCSMs),[38] the phase of which provides estimates of the directivity of the maximum source region.[39] The SCSM also provides a means to estimate the source self-coherence along the source distribution. The SCSMs are compared across three power conditions to show how source levels and coherence properties vary. In addition, an analysis of the sideline and downstream noise sources is performed to understand the respective source levels and coherence properties corresponding to large and fine-scale radiation structure spectra.[40] When the sideline and downstream portions of the linear array are processed separately with the HM, strong distinctions of the SCSMs are manifested. Complementing source level estimates with source coherence analyses better characterize the full-scale jet noise radiation and thus can serve as a benchmark for similar lab-scale and computational jet noise studies.

II. METHODS

The large length scales of turbulent mixing noise from a tactical engine produce partially correlated sound radiation, thus requiring a partially correlated source model. Advanced beamforming methods (with strong ties to identification methods) have been developed that solve for the potential sources simultaneously (see Ref. 35) and thus provide a means of investigating and modeling source correlation features. Examples of correlated and partially correlated noise source mapping methods include DAMAS-C[15] and derivatives (that require fewer iterations),[38] covariance matrix fitting for correlated sources (CMF-C and MACS),[34,41] the SODIX method for modeling source directivity,[22] LORE modified for coherent sources,[42] L_1 generalized inverse beamforming (L_1-GIB)[33] and its derivatives [e.g., GWIB (Refs. 43, 44) and GINV (Ref. 17)], and more recently the HM (Ref. 18). A more exhaustive review of the various methods can be found in Refs. 2, 5, and 6. These methods also provide information about the self-coherence along a distributed source, which is useful to study the source composition, including its phase speed. The results can also be used as an equivalent source model to predict the levels and coherence properties of the radiation.

A previous numerical validation study[35] compared a subset of the aforementioned techniques, including cross beamforming (a precursor to DAMAS),[25] functional beamforming,[45] HM, GINV, and MACS techniques. It was found that all methods adequately estimated the source levels for the scenarios tested. However, the HM showed the best overall performance in estimating the source levels and coherence properties and has been selected as the method most suitable for the current problem. In Sec. II A, the HM is reviewed, followed by a summary of the UPAINT method's implementation in Sec. II B.

A. Review of hybrid method

Assuming m measurement points and s potential source locations, the HM attempts to solve a least-squares minimization problem from

$$\mathbf{p} = \mathbf{G}\,\mathbf{q}, \tag{1}$$

where the vector of known complex acoustic pressures, $\mathbf{p}$, for a given frequency, f, is $[m, 1]$ in size, and the vector of unknown complex source strengths, $\mathbf{q}$, is $[s, 1]$. The source strengths are volume velocities with units of m^3/s. The Green function matrix, $\mathbf{G}$, is comprised of steering vectors along the columns such that

$$\mathbf{G} = \begin{bmatrix} \mathbf{g}_{i=1} & \dots & \mathbf{g}_{i=s} \end{bmatrix}, \tag{2}$$

and accounts for the free-field monopole propagation from each source location to each measurement position. In Eq. (2), each steering vector, $\mathbf{g}_i$, is comprised of steering elements from the potential source location, $\vec{r}_i$, to each measurement location.

Many techniques are available to solve Eq. (1), but a common method is to employ a Moore–Penrose pseudoinverse coupled with a regularization approach.[18,46] Traditional Tikhonov regularization improves the conditioning of $\mathbf{G}^{\mathrm{H}}\mathbf{G}$ by supplementing it with a penalization parameter, ν^2, along the diagonal entries as

$$\mathbf{q}_{\mathrm{Tikhonov}} = (\mathbf{G}^{\mathrm{H}}\mathbf{G} + \nu^2\mathbf{I})^{-1}\mathbf{G}^{\mathrm{H}}\mathbf{p}, \tag{3}$$

where $\mathbf{I}$ is the identity matrix and ν^2, the penalization parameter, is determined by various means, including the Morozov discrepancy principle and generalized cross validation.[23] However, the HM regularization is a modification beyond standard Tikhonov regularization. In HM the penalization parameter is added to a square weighting matrix, and the solution to Eq. (1) then becomes

$$\mathbf{q}_{\mathrm{HM}} = (\mathbf{G}^{\mathrm{H}}\mathbf{G} + \nu^2\mathbf{L}^{\mathrm{H}}\mathbf{L})^{-\mathbf{1}}\mathbf{G}^{\mathrm{H}}\mathbf{p}, \tag{4}$$

where $\mathbf{L}$ is a beamforming regularization matrix,

$$\mathbf{L}^{-1} = \mathrm{Diag}\left(\frac{\sqrt{\mathrm{diag}(\mathbf{Q}_{\mathbf{CBF}})}}{\sqrt{\|\mathrm{diag}(\mathbf{Q}_{\mathbf{CBF}})\|_\infty}}\right). \tag{5}$$

In Eq. (5), the notation $\mathrm{diag}(\cdot)$ takes the diagonal elements of a matrix and $\mathrm{Diag}(\cdot)$ forms a diagonal matrix of these elements, $\|\cdot\|_\infty$ is the infinity norm, and $\sqrt{\cdot}$ is applied element-wise. The square matrix, $\mathbf{Q}_{\mathbf{CBF}}$, consists of cross-spectral elements formed from the individual source strengths of a conventional beamforming (CBF) solution. The CBF matrix solution is

$$\begin{aligned} \mathbf{Q}_{\mathbf{CBF}} &= \mathbf{q}_{\mathbf{CBF}}\mathbf{q}_{\mathbf{CBF}}^{\mathrm{H}} \\ &= \left(\mathbf{G}_{\mathbf{SV}}^{\mathrm{H}}\,\mathbf{p}\right)\left(\mathbf{G}_{\mathbf{SV}}^{\mathrm{H}}\mathbf{p}\right)^{\mathbf{H}} \\ &= \mathbf{G}_{\mathbf{SV}}^{\mathrm{H}}\mathbf{p}\mathbf{p}^{\mathbf{H}}\mathbf{G}_{\mathbf{SV}}, \end{aligned} \tag{6}$$

where the steering vector matrix, $\mathbf{G}_{\mathbf{SV}}$, is

$$\mathbf{G}_{\mathbf{SV}} = \left[\frac{\mathbf{g}_{i=1}}{\|\mathbf{g}_{i=1}\|}, \dots, \frac{\mathbf{g}_{i=s}}{\|\mathbf{g}_{i=1}\|}\right], \tag{7}$$

with $\|\cdot\|$ as the L_2 norm.

The use of $\mathbf{L}$ in the beamforming regularization matrix [Eq. (5)] is an improvement to the standard regularization process because the Green function matrix is weighted by the CBF solution to add *a priori* information about the beamforming source locations to more selectively penalize the source region instead of the source-independent approach of classical Tikhonov regularization. This allows the noise threshold to vary in space as a function of the precomputed CBF levels so that regions where acoustic sources are absent are more strongly regularized. In fact, the incorporation of the beamforming results into $\mathbf{L}$ resembles the L_p norm formulation in Ref. 33, although the current method does not require iteratively reweighted least squares techniques to solve. Incorporating Eq. (5) into Eq. (4) and simplifying produces

$$\tilde{\mathbf{q}}_{\mathrm{HM}} = \mathbf{L}^{-1}\left(\underline{\mathbf{G}}^{\mathbf{H}}\underline{\mathbf{G}} + \nu^2\mathbf{I}\right)^{-1}\underline{\mathbf{G}}^{\mathbf{H}}\mathbf{p}, \tag{8}$$

where $\underline{\mathbf{G}} = \mathbf{G}\mathbf{L}^{-1}$, and $\tilde{\mathbf{q}}_{\mathrm{HM}}$ is the estimated vector of (complex) source strengths. Using Eq. (8), HM is developed such that

$$\mathbf{Q}_{\mathbf{HM}} = \tilde{\mathbf{q}}_{\mathrm{HM}}\tilde{\mathbf{q}}_{\mathrm{HM}}^{\mathbf{H}} = \mathbf{L}^{-1}\beta\left(\mathbf{J}\,\underline{\mathbf{G}}^{\mathbf{H}}\right)\mathbf{C}\left(\underline{\mathbf{G}}\,\mathbf{J}^{\mathbf{H}}\right)\beta^{*}\left(\mathbf{L}^{-1}\right)^{\mathbf{H}}, \tag{9}$$

where $\mathbf{C} \equiv \langle \mathbf{p}\mathbf{p}^{\mathbf{H}} \rangle$ is the cross-spectral matrix (CSM) derived from the array pressures, $\mathbf{p}$ (with $\langle\cdot\rangle$ denoting a time average), and

$$\boldsymbol{J} = \left(\underline{\mathbf{G}}^{\mathbf{H}}\underline{\mathbf{G}} + \nu^2\mathbf{I}\right)^{-1}. \tag{10}$$

In Eq. (9), a scaling term, β, is included, where

$$\beta = \|\underline{\mathbf{G}}^{\mathbf{H}}\underline{\mathbf{G}} + \nu^2\mathbf{I}\|, \tag{11}$$

to compensate for the addition of regularization, which can affect the accuracy of the overall levels.

The regularization parameter, ν^2, requires consideration as it is responsible for smoothing values that approach the noise levels contained in the measurement data. Padois *et al.*[18] conducted a regularization study using HM and found that by setting ν^2 to be at least 5% of the largest eigenvalue of $\mathbf{G}^{\mathrm{H}}\mathbf{G}$, the sound source level converged to the correct levels, with the source levels being overestimated for smaller regularization values. The 5% threshold was similarly used in this study. This threshold corresponds to the value for which eigenvalues of $\underline{\mathbf{G}}$ that are below this threshold are orders of magnitude lower (i.e., near the noise floor of the measurement; see Ref. 35). For frequencies at or below the array spatial Nyquist frequency of the array, this recommendation was appropriate.

B. Review of UPAINT algorithm

The upper limit to the usable bandwidth for frequency-domain phased-array processing is set according to the spatial Nyquist frequency of a uniform input array. This is determined by solving for the frequency at which the array interelement spacing equals one-half wavelength. Phased-array results above this limit introduce grating lobes, which are effectively spatially aliased estimates of the source properties. Where inverse and regularization methods are applied, these grating lobes may interfere with the estimation process by redistributing energy from the true source estimate location to the grating lobes, or vice versa. To ameliorate the source estimates, a method was developed by Goates *et al.*[36] to increase the frequency bandwidth for the beamforming of broadband sources. A summary of the method is presented here, and a detailed description of the process is given in Ref. 36. This study represents the first application of the UPAINT method to jet noise source analysis.

The UPAINT method effectively creates a higher-density interpolated array to increase the spatial Nyquist frequency so that grating lobes do not interfere with the beamforming estimates. The idea of array interpolation and/or extrapolation is not new.[47] For example, a similar method, "Bayesian focusing,"[48] adds *a priori* information about the source characteristics (including location) to better constrain a set of radiation basis functions, which result from smoothly interpolating across the array measurements. This results in a focused reconstruction region and improves the source resolution (i.e., a higher frequency reconstruction) beyond the spatial Nyquist. However, it requires careful selection of the source dimensions and region, in addition to rejecting noise associated with the interpolation. The UPAINT process instead achieves this result by operating on both the frequency-dependent cross-spectra, $\mathbf{C}_{i_1,i_2}(f)$, of each microphone pair and the entire cross-spectral matrix of each frequency. First, the cross-spectral phase, $\mathbf{\Phi}_{i_1,i_2}(f)$, is determined for each element of $\mathbf{C}$, where

$$\mathbf{\Phi}_{i_1,i_2}(f) = \arg\left[\mathbf{C}_{i_1,i_2}(f)\right], \tag{12}$$

and i_1 and i_2 correspond to two array elements. Next $\mathbf{\Phi}_{i_1,i_2}(f)$ is unwrapped for each microphone pair to provide a smoothly varying phase. This is done using a coherence-based unwrapping procedure described in Ref. 49, which was implemented previously on lab-scale rocket measurements for intensity-based measurements.[37] The resultant unwrapped phase matrix, $\tilde{\mathbf{\Phi}}(f)$, contains the unwrapped phase of each array microphone pair. Together, the magnitude matrix, $|\mathbf{C}(f)|$, and $\tilde{\mathbf{\Phi}}(f)$ form the two components of the UPAINT cross-spectral matrix. The separated the cross-spectral matrix components, $|\mathbf{C}(f)|$, and $\tilde{\mathbf{\Phi}}(f)$, are smoothly varying and hence can be interpolated. Both matrices are interpolated to the desired spatial locations to increase the spatial Nyquist frequency of the array. The interpolated components of $|\mathbf{C}(f)|$, and $\tilde{\mathbf{\Phi}}(f)$ are then combined elementwise as

$$\mathbf{C}_{\mathbf{UP}_{i_1 i_2}}(f) = |\mathbf{C}_{\mathrm{interp}_{i_1 i_2}}(f)| \cdot \exp\left[j \cdot \tilde{\mathbf{\Phi}}_{\mathrm{interp}_{i_1 i_2}}(f)\right]. \tag{13}$$

The matrix $\mathbf{C}_{\mathbf{UP}}(f)$ is then input into the HM algorithm as a standard cross-spectral matrix; $\mathbf{C}_{\mathbf{UP}}$ is used in place of $\mathbf{C}$ in Eq. (9) for the HM.

Because the array is interpolated—usually such that the interelement spacing corresponds to a spatial Nyquist frequency above the frequencies of interest—the HM results do not contain grating lobes that can interfere with the source

estimates. However, special considerations are needed for the regularization parameter for the HM. Above the spatial Nyquist frequency of the array it was found that the 5% eigenvalue threshold would overpredict the value at which the eigenvalue drop occurred, thus leading to overregularization. An attempt to more precisely determine the threshold value was made by determining the critical eigenvalues of $\underline{\mathbf{G}}$. For example, the threshold can be estimated by determining the last eigenvalue for which

$$|d\boldsymbol{\lambda}_{\underline{\mathbf{G}}}/dx| > \mathrm{std}\big(\mathrm{abs}\big(d\boldsymbol{\lambda}_{\underline{\mathbf{G}}}/dx\big)\big)/2, \tag{14}$$

where $d\boldsymbol{\lambda}_{\underline{\mathbf{G}}}/dx$ takes the finite difference along, $\boldsymbol{\lambda}_{\underline{\mathbf{G}}}$, which are the eigenvalues of $\underline{\mathbf{G}}$ (in descending order), and $|\cdot|$ and std$(\cdot)$ are the absolute value and standard deviation operators, respectively. Equation (14) was determined empirically and—for frequencies at or below the array spatial Nyquist frequency—produces ν^2 values that are approximately those found using the recommendation of Padois *et al.* However, above the array spatial Nyquist frequency, the ν^2 value is more closely associated with the turning point at which the eigenvalues of $\underline{\mathbf{G}}$ begin to significantly deviate from the standard deviation value. While more robust methods for determining this threshold are available,[48,50] Eq. (14) was sufficient for the current study.

III. RESULTS

The HM and UPAINT methods described in Sec. II are applied to noise measurements taken of a full-scale tactical engine. The experimental setup is described in Sec. III A. In Sec. III B, measurements from a ground-based linear array are input to the HM to estimate equivalent source characteristics with the engine operating at 100% (military power), and the UPAINT method is applied for frequencies above the spatial Nyquist frequency of the input array. The HM results are validated by comparing separate measurements taken about midway between the source and the linear array with estimates from an HM-based equivalent source model. In addition, an HM-based source cross-spectral matrix is calculated to estimate the source properties, including the convective phase-speed and the coherence properties across the source. In Sec. III E, the measurement array is subdivided into two components to identify the source levels and coherence properties associated with sound radiating perpendicular to the jet centerline, as well as the source properties related to the maximum radiation region. Finally, Sec. III F provides an analysis of the HM results for two engine powers, including 25% and afterburner conditions, and the results are compared to the 100% power condition reported in Sec. III B. The goal of these analyses is to provide a more complete profile of jet noise source properties and accompanying radiation for full-scale tactical aircraft.

A. Experiment

Noise measurements were taken of an installed full-scale tactical engine (see Fig. 1) that was run at three different conditions, namely, intermediate [INTER; $25 \pm 3\%$ Engine Thrust Request (ETR)], military (MIL; $100.0 \pm 0.2\%$ ETR) and afterburner (AB; $150.0 \pm 0.2\%$ ETR), while the other engine on the tied-down aircraft was held at idle. While a summary of the experiment is provided here, and a detailed description can be found in Ref. 21, and the spectral variation of the measured sound as a function of angle is shown in Ref. 40. An array of 50 GRAS 6.35- and 3.18-mm microphones was placed on the ground 11.6 m from the centerline of the jet axis. As shown in Fig. 1, the ground array spanned 30 m and the array element spacing was 0.61 m—except for a small gap in the array towards the downstream end. No effort was made to correct for this array gap (e.g., interpolate measurements at locations within the array gap) due to the near-grazing incidence of the sources on the array at that location (except as done using UPAINT above the spatial Nyquist frequency). A separate two-dimensional *scanning* array—consisting of 90 microphones in a 5×18 element pattern and uniformly spaced with a 15.2 cm inter-element spacing—was used for ten nonsynchronous measurements at array locations parallel to the jet shear layer and marked by the triangles in Fig. 1. A subset of 18 array elements (i.e., a single row from the scanning array) were extracted from each of the ten scan locations, forming an equivalent one-dimensional array 0.38 m above the ground and parallel to the shear layer. These measurements are cumulatively referred to as the *scan line*. For each of the nonsynchronous scanning array measurements, measurements were also taken at the ground array.

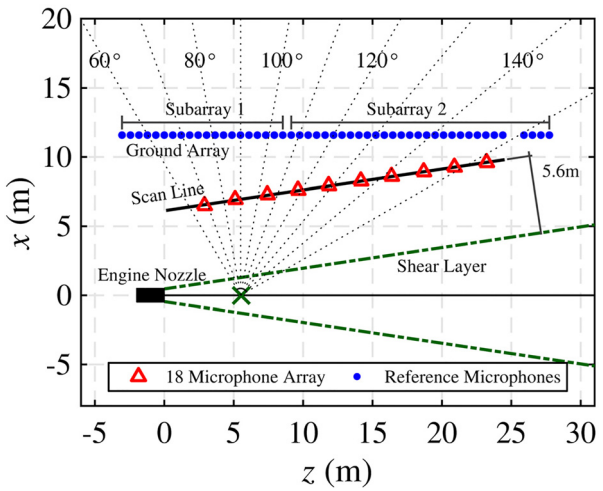

FIG. 1. (Color online) Schematic of the experimental setup. A ground-based array of 50 microphones is shown with blue dots and the 18-element scanning array was moved to locations marked by red triangles. Inlet angles are measured relative to the microphone array reference point (MARP) indicated by the green x.

The ground array measurements were processed to obtain the cross spectral calculations for the HM algorithm. Each 30 s measurement had either a 48 or 96 kHz sampling rate, depending on the engine condition tested, and each resultant waveform was divided into time-waveform blocks of 16 384 samples each with 50% overlap. Due to the low variation of the statistics from measurement to measurement (see Fig. 8 of Ref. 21), the ten ground array measurements that were taken while the scanning array was moved were appended to form a single 300 s measurement. A Fourier

transform was applied after each block was filtered by a Hann window, and cross-spectral calculations were averaged over the blocks to obtain cross-spectral density elements. These elements form a cross spectral matrix, **C**, for each frequency at the ground array measurements to serve as inputs to the HM. Whereas some studies apply a diagonal deletion to **C** to reduce microphone self-noise,[51] particularly for cases when flow noise is present, this deletion was not applied here as the source measurement levels were on the order of at least 30 dB higher than background and flow noise levels.

One-third octave (OTO) band levels of the measurements at the ground-based measurement array are displayed in Fig. 2 for three engine conditions. In each case, the maximum radiation region varies with frequency and shifts upstream—towards the sideline—with increasing frequency. The maximum radiation region at INTER is primarily located far downstream at 100 Hz and does not seem to be fully captured by the array, although the peak levels at 400 Hz are at a position of about $z = 8$ m. At MIL, the peak levels are about 30 dB higher than INTER, and two distinct radiation lobes are present in the ground array data, centered at $z = 20$ m and 125 Hz and $z = 12.5$ m and 500 Hz, respectively. These radiation lobes extend many meters spatially as well as across multiple one-third octave bands. These multiple lobes have been observed in other full-scale studies as well, including from far-field acoustical noise measurements collected from installed engines on the F-35 (Ref. 52) and the F-18.[53] At AB in Fig. 2(c), the results are like the MIL spectra, except that the levels are about 4–6 dB higher overall, and the peak level locations are farther upstream, along the array. The primary lobe is shifted upstream to about $z = 17.5$ m. Evidence of multiple lobes—including a possible third lobe at $z = 10$ m and 500 Hz—is present, located about 2 m farther upstream compared to the lobes at MIL. The origins of these multilobe features are under investigation. It has been hypothesized that they are the result of broadband shock-associated noise due to shock cells interacting with turbulence structures,[54–56] and the effect of high temperatures to separate Mach wave and large-scale structure radiation.[31] In addition, both MIL and AB spectra contain a peak in the spectra at $z = -2$ m and 800 Hz, and similar features have been associated to broadband shock-associated noise.[29] In Sec. III B, the MIL CSM is the HM input and resulting source distributions are shown. Results for the INTER and AB cases are considered in Sec. III F.

A comparison of the noise at the different tactical engine conditions with laboratory-scale jets was provided in Ref. 29 and includes jet noise classifications based on maximum radiation angle, the scaling of peak Strouhal number according to the maximum radiation direction, and geometric scaling based on nozzle diameter. It was found that for the INTER engine condition the overall radiation angle of approximately 150° suggests the jet noise acts similar to convectively subsonic laboratory-scale jet. For the AB case, however, the maximum radiation angle is approximately 125°, indicating a convective Mach number of approximately 1.7–1.8. They also found that for prior supersonic engine tests by Greska[57] and by Schlinker *et al.*,[9] the peak Strouhol number is 0.15–0.30. These findings suggest that, for the present study, an appropriate frequency-to-Strouhol number scaling is about $1.2 \cdot 10^{-3}\text{Hz}^{-1}$. These results corroborate similar findings for heated supersonic jet measurements that approach settings found in typical full-scale tactical jet measurements.[57–62]

B. Beamforming at military power

The CSM at MIL engine power—corresponding to the OTO levels shown in Fig. 2(b)—are used as inputs for the HM to yield estimated source levels as a function of frequency.

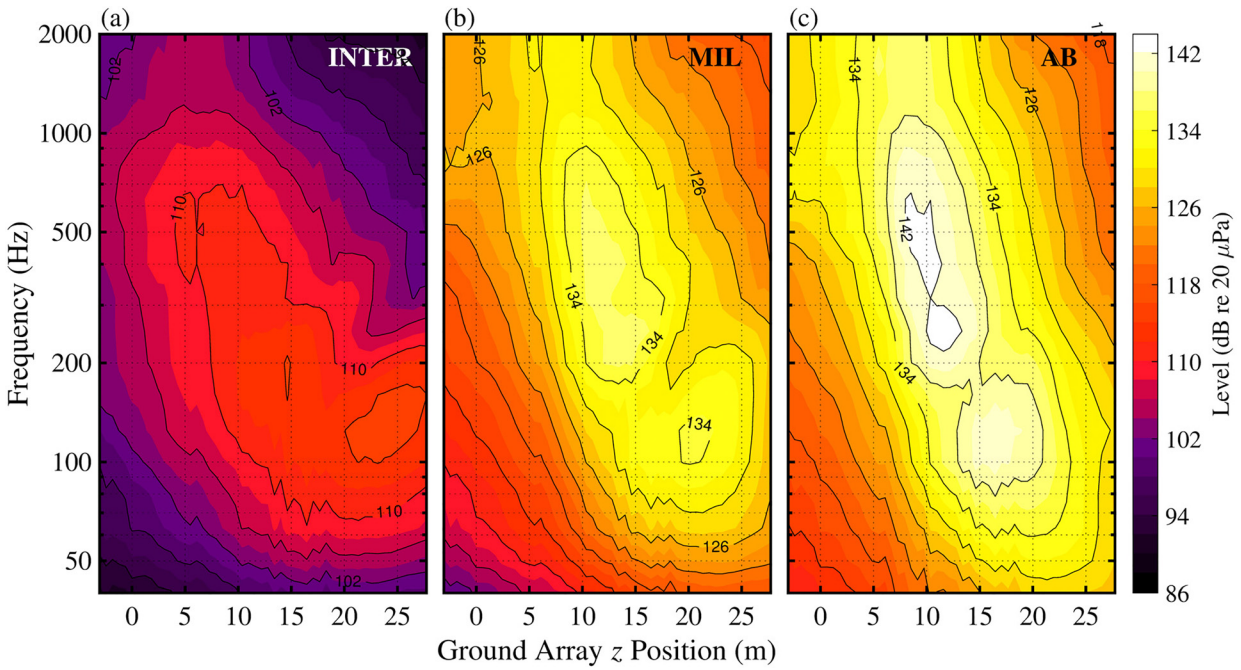

FIG. 2. (Color online) One-third octave band levels at (a) INTER, (b) MIL, and (c) AB engine condition along the ground-based measurement array.

The resulting source distributions are shown in Fig. 3(a), across the axis of the jet centerline (shown as a black solid line in Fig. 1) at the nozzle height of 1.9 m. The distribution is discretized at 10 cm intervals for all HM results, and the OTO center-band results were obtained by summing over appropriate 5.9 Hz narrowband values. Colored areas and black contour lines represent the source strength densities (i.e., a spatial density), while the white contour lines represent equal-level contours relative to the peak level at each frequency. The source strength densities, $\mathbf{q}_{\mathrm{HM}} \equiv \sqrt{\mathrm{diag}(\mathbf{Q}_{\mathrm{HM}})}$, are absolute level estimates having units of a volume velocity per unit meter (along the jet centerline), and they are shown in dB using an arbitrary reference of $10^{-3}\,\mathrm{m}^3/\mathrm{s}$. As seen in lab-scale and full-scale beamforming measurements,[11,14,19] as well as for acoustical holography[55] and vector-intensity-based source estimates,[63] the source distribution shifts upstream and the extent of the source diminishes with increasing frequency. These effects are best visualized using the white 3 dB-down contour lines in Fig. 3(a).

The measurement array used in this study has a spatial Nyquist frequency at about 280 Hz, due to the 0.61 m interelement spacing, and grating lobes begin to interfere with the source estimates above this frequency. To increase the usable bandwidth of the measurement array for beamforming studies, UPAINT processing was applied in Fig. 3(b) to all frequencies above the spatial Nyquist frequency (>280 Hz). While the UPAINT algorithm removed grating lobes for frequencies above 550 Hz, it is believed that substantial noise within $\mathbf{C}$ strongly affected the UPAINT algorithm for a band of frequencies between 280 and 550 Hz so as to fail to remove the grating lobes. Therefore, a supplemental spatial unwrapping of the phase of $\mathbf{C}$ was necessary to remove additional artifacts. As shown in Fig. 3(b), the additional spatial unwrapping seems to improve the results.

The HM and UPAINT-HM results—$\mathbf{q}_{\mathrm{HM}}$ and $\mathbf{q}_{\mathrm{U-HM}}$, respectively—are shown alongside each other in Fig. 3. Without UPAINT, grating lobes appear in $\mathbf{q}_{\mathrm{HM}}$ results above about 400 Hz and progress towards the main lobe with increasing frequency. In addition, the source levels decline with increasing frequency, and it is likely that the HM algorithm distributes the energy of the main lobe to the additional grating lobes. The normalized contour lines (overlain in white) show the source extent as a function of level, relative to the peak level. For example, the white 6 dB down contour lines show that without UPAINT the grating lobes significantly affect the main source distribution above 1000 Hz. In addition, the source contracts significantly past the spatial Nyquist frequency.

With UPAINT and the additional spatial unwrapping applied at select frequencies, the grating lobes effects in the HM results are not present in the UPAINT-HM source estimates. The source extent and location of $\mathbf{q}_{\mathrm{U-HM}}$ results, measured using the normalized 6-dB down contour lines, are qualitatively similar to the $\mathbf{q}_{\mathrm{HM}}$ results, although some differences do exist. For example, as measured using the 6 dB contour lines, the frequency-dependent source extents of the $\mathbf{q}_{\mathrm{U-HM}}$ are slightly larger than those of $\mathbf{q}_{\mathrm{HM}}$—e.g., the $\mathbf{q}_{\mathrm{U-HM}}$ extent at 800 Hz is about 7.5 m compared to the corresponding $\mathbf{q}_{\mathrm{HM}}$ extent of 5.5 m. Further study is necessary to definitively quantify the source extent above the spatial Nyquist frequency as the $\mathbf{q}_{\mathrm{HM}}$ source extent may be contracted due to aliasing while the UPAINT process may be enlarging the $\mathbf{q}_{\mathrm{U-HM}}$ source extent slightly. However, because

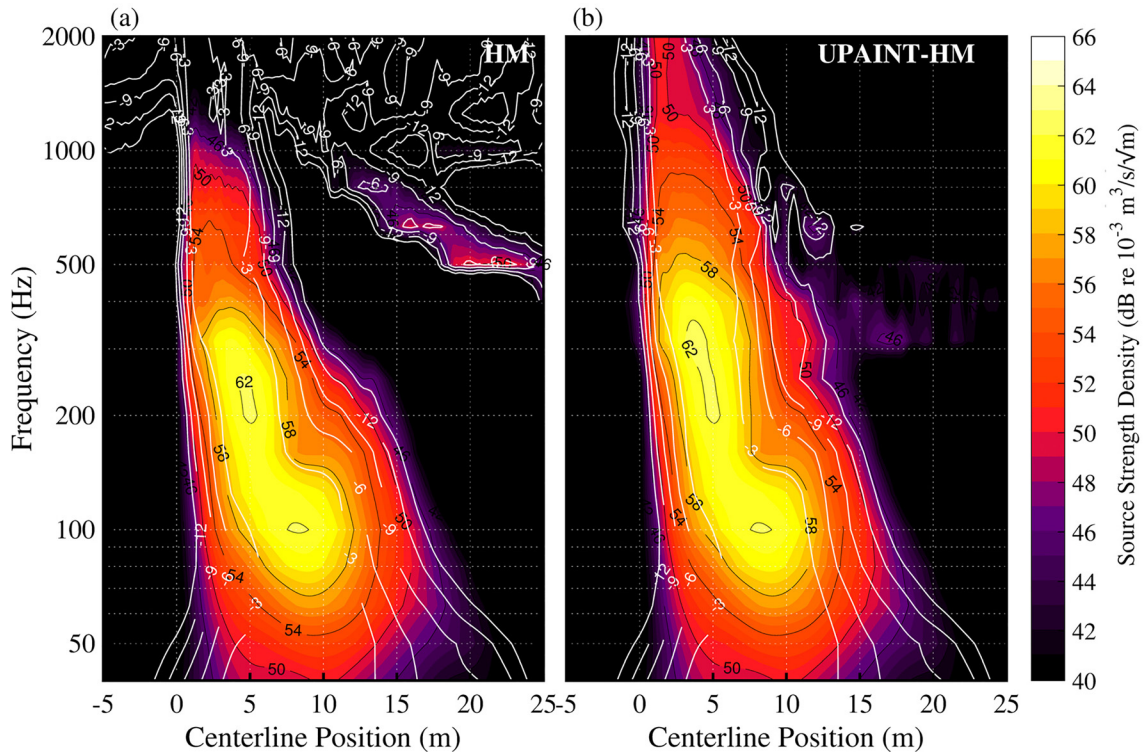

FIG. 3. (Color online) Source strength density, $\mathbf{q}_{\mathrm{HM}}$, via (a) HM and (b) UPAINT-HM along the jet centerline using ground-array measurements of tactical aircraft noise at MIL engine condition. The colors and black contour lines indicate absolute levels, and the white contour lines indicate the levels relative to the maximum level of each one-third octave band.

the UPAINT-HM results remove the extraneous grating lobes, the UPAINT-HM results can be used as an equivalent source model (ESM) above the spatial Nyquist frequency to provide estimates of the sound field. This predictive capability is used here to substantiate the source model.

These results can be compared to the limited full-scale jet noise phased-array source characterizations in the literature. Schlinker *et al.*[9] showed beamforming source estimates of an uninstalled, full-scale, tactical aircraft engine using measurements taken in the maximum radiation direction with a compact 3.9 m ground-based array. They applied the integration beamforming approach of Ventakesh *et al.*[7] and found the maximum source location when the engine operated at AB is centered approximately 4–6 nozzle diameters (D) downstream for frequencies between 250 and 400 Hz. Using an approximate nozzle diameter of 0.6 m (see Ref. 29), the maximum source locations, based on the results in Fig. 3 for this installed, full-scale, tactical aircraft engine operating at MIL, are centered between 6 and 8 D, which is slightly farther downstream than found by Schlinker *et al.* In addition, a primary and secondary lobe are visible in the source estimates, similar to the features seen in the spectral levels at the ground array [see Fig. 2(b)]. The primary lobe in Fig. 3(b) peaks at 8 m at 100 Hz, and the secondary lobe peaks at about 5 m at 250 Hz. The source extent greatly contracts and shifts upstream between these two features.

C. Equivalent source model validation

A validation of the UPAINT-HM results is performed by treating the HM-based source results, $\mathbf{Q}_{\mathrm{HM}}$, as an ESM to generate a predicted sound field using a Rayleigh integration. Here, the ESM for MIL has been used to predict the sound pressure level as a function of frequency along the scan line in Fig. 1. It should be stressed that the scan line measurements are not used as phased-array inputs and therefore serve as an independent verification for the HM-UPAINT-based ESM. The spectral levels along the scan line are shown in Fig. 4(a). Because the scan line measurements were taken at a height of 0.38 m above a concrete surface, an interference null is present. The null begins at 700 Hz at $z = 2$ m and shifts up in frequency to about 2000 Hz and $z = 17$ m. To account for the ground reflection in the HM-based ESM, an image source of the ESM is created at a height, $y = -1.9$ m, and the HM results, $\mathbf{Q}_{\mathrm{HM}}$, are reduced by a factor of two to account for pressure doubling at the ground surface.

The ESM-predicted levels along the scan line are shown in Fig. 4(b), and the error between the measured and predicted spectral levels is provided in Fig. 4(c). There is good agreement between the measured and predicted levels overall, particularly for frequencies between 100 and 500 Hz where errors are mostly less than 2 dB. Under 100 Hz, the predicted levels underestimate measured levels by about 2 dB. In addition, the predicted levels have significantly deeper interference nulls, as indicated by the large errors above 500 Hz that in some cases exceed 10 dB. Because the ESM and its image are line source distributions, they do not adequately represent the more complex sound radiation created by a volume source and its interference with a hard surface. This underprediction of the levels in an interference null is also observed in near-field acoustical holography results, and Leete *et al.*[64] observed low correlation between

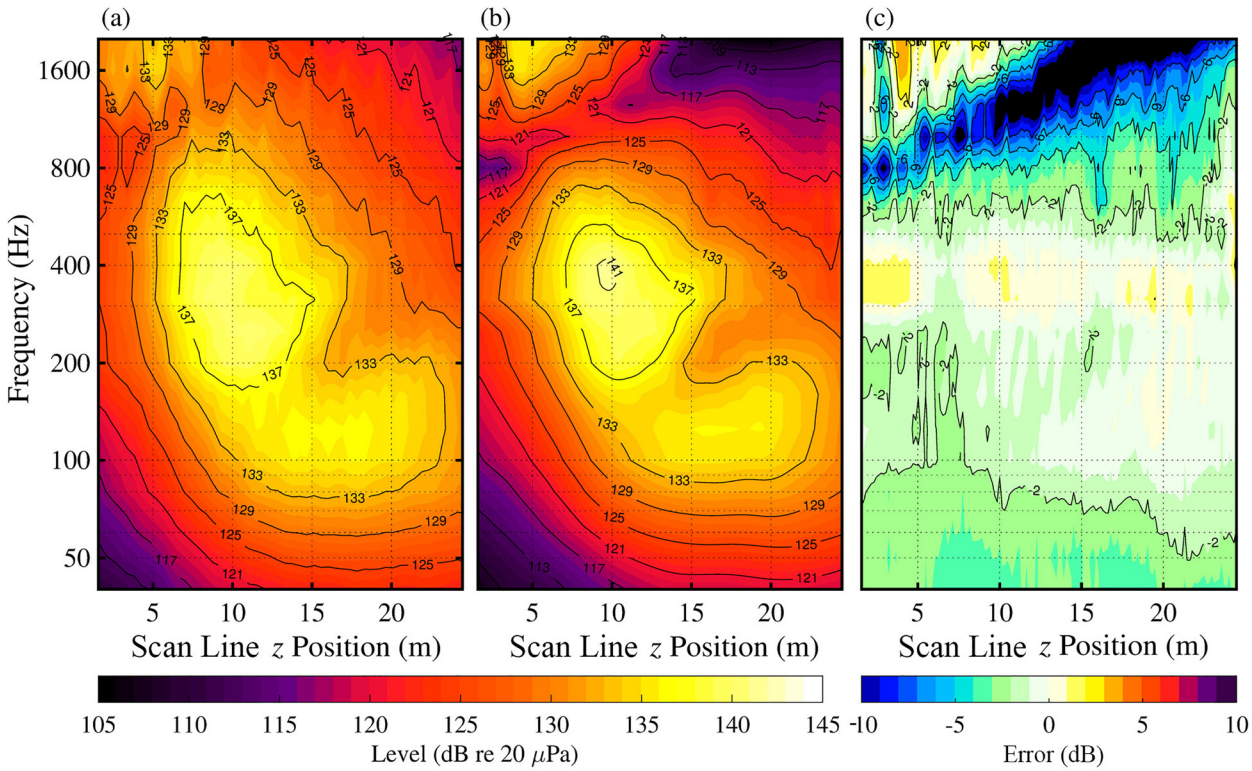

FIG. 4. (Color online) (a) One-third octave band level measurements at scan line at MIL engine condition, (b) predicted levels from HM-based equivalent source model, and (c) the difference between the predicted and measured levels.

destructive and constructive interference regions of such measurements. Overall, the predicted levels agree with those measured closer to the centerline, and at an elevated height, thus, providing a measure of validation to the HM results.

D. Source model phase and coherence estimates

Looking beyond strictly level-based results, the HM results, $\mathbf{Q}_{\mathrm{HM}}$, are a source cross spectral matrix (SCSM) that can lend insights into phase of the equivalent acoustic source. To provide examples, the unwrapped phase, referenced to the peak source level location, is shown in Figs. 5(a) and 5(b) for 100 and 200 Hz for MIL power. The slope of the unwrapped phase can be related to the convective phase speed—and consequently the radiation directivity—of an equivalent propagating wave across the source distribution. Thus, the radiation directivity can be approximated from the slope of the unwrapped phase. At 100 Hz [Fig. 5(a)], the unwrapped phase is matched by a reference line (dashed black line) that has a −1.28 rad/m slope, corresponding to a plane wave propagating with a directivity of 135°, measured relative to the engine inlet in Fig. 1. The slope of this line closely resembles the phase of the HM results between about $0\,\mathrm{m} \leq z \leq 15\,\mathrm{m}$, coinciding well with the peak source levels [Fig. 3(b)]—the top 15 dB of which is overlaid on Fig. 5(a) for convenience. A similar analysis at 200 Hz [Fig. 5(b)] shows that a reference line with a slope of −2.07 rad/m matches the phase of the HM source distribution near the peak level location, corresponding to a directivity of 125°. The slope of the phase, however, only matches the reference line across the top 3 dB of the source region. Outside of this region, the phase is steeper for $z < 2$ m and more gradual for $8\,\mathrm{m} < z < 15\,\mathrm{m}$. Thus, at 200 Hz the radiation is not as unidirectional as at 100 Hz, which is confirmed by the additional spectral features (e.g., multilobe radiation[40]) in the ground-based array measurements. Additionally, the phase speed changes erroneously for $z > 15$ m, where source levels are 15 dB below the peak level, likely a processing artifact of a noise-dominated unwrapping process.

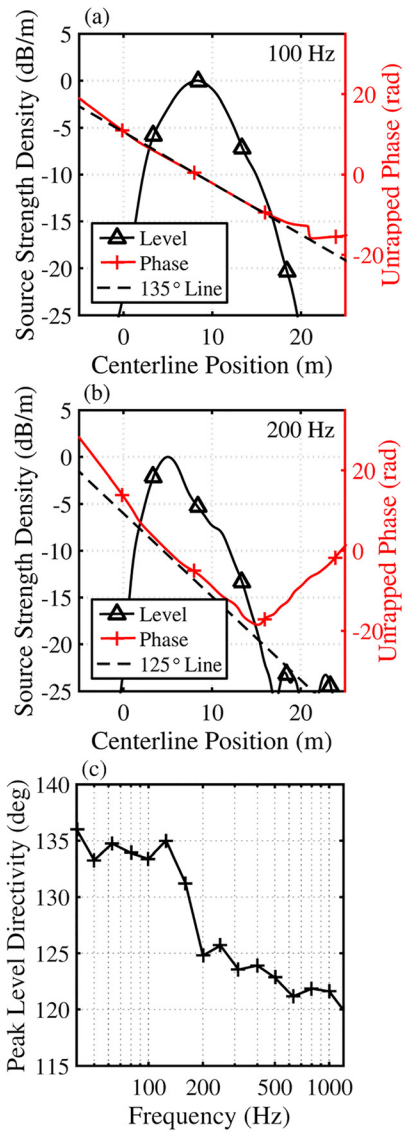

FIG. 5. (Color online) Hybrid method results, $\mathbf{q}_{\mathrm{HM}}$, (triangles) at (a) 100 Hz and (b) 200 Hz at MIL engine condition and the unwrapped phase of the source calculated relative to the maximum source level location (plus signs) and a reference line (dashed) corresponding to the directivity indicated in the legend. (c) Directivity angle (relative to the engine inlet) estimated from the slope of the unwrapped phase in the vicinity of the peak source levels as a function of frequency.

These examples show that the SCSM can be used to estimate the prominent radiation directivity at which the HM results would radiate if treated as an equivalent source. An estimate of the SCSM angle directivity as a function of frequency is given in Fig. 5(c); the estimated directivity was calculated as in the examples of 100 and 200 Hz by matching the slope of the SCSM phase in the vicinity (i.e., ±0.2 m) of the peak source level locations. The plotted directivity is primarily 135° for frequencies up to 125 Hz followed by a rapid transition to a 125° directivity at 200 Hz and a gradual shift to about 120° at 1000 Hz. The trends agree with the peak spectral level locations in Fig. 2(b), which are relatively fixed up to 125 Hz before transitioning rapidly upstream at about 160 Hz and then which gradually shift slightly farther upstream with frequency above 200 Hz.

The frequency-dependent spatial variation in levels ($\mathbf{q}_{\mathrm{HM}}$) and examples of the relative phase across the ESM can reproduce measured levels and match directivity but have not described the source self-coherence. Source self-coherence identifies the nature of the source as a coherent, partially coherent or incoherent distribution. Source self-coherence can be calculated by normalizing off-diagonal elements of the SCSM by the corresponding diagonal elements, and estimates are shown in Figs. 6(a)–6(c) for frequencies of 100, 200, and 500 Hz. The corresponding $\mathbf{q}_{\mathrm{HM}}$ values are shown in Figs. 6(d)–6(f). In each case, dashed lines are overlaid on the coherence plot and HM source levels plot to show the point at which the source levels are 12 dB down from the maximum level at that frequency. The dashed-line box helps to separate coherence results where the levels are high from those elements of the SCSM that may be contaminated by noise; the 12 dB threshold level was empirically selected. As shown in Fig. 6(a), the source coherence at 100 Hz has values ≥ 0.5 over a spatial region that extends at least 4 m in either direction from the peak level location, $z \approx 8$ m. This region of high coherence encompasses over 50% of the top 12 dB of the source distribution, characteristic

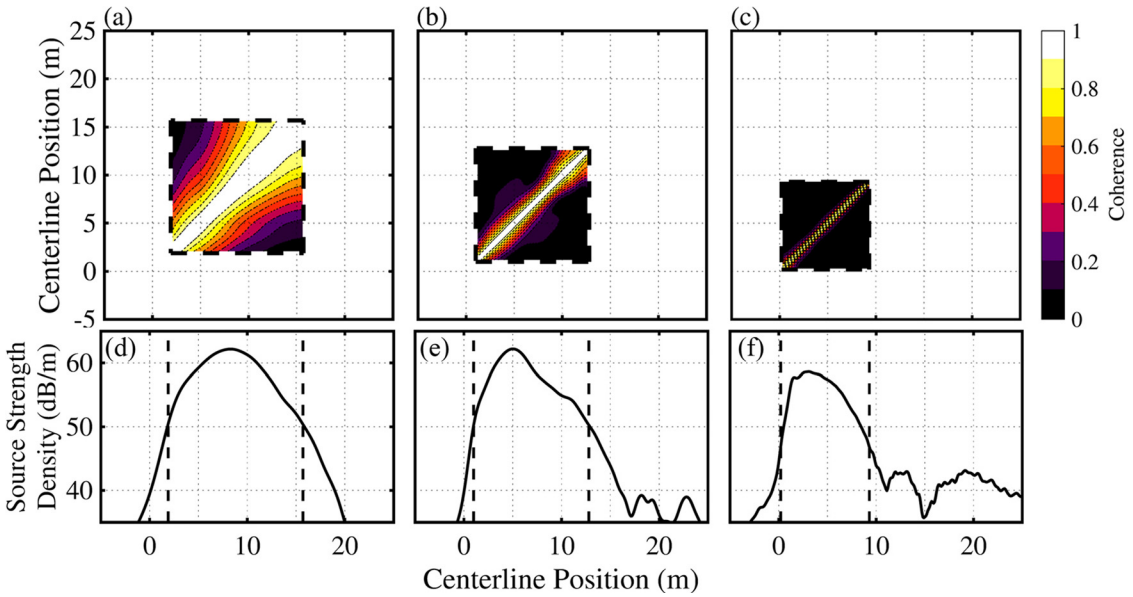

FIG. 6. (Color online) HM-based source coherence and corresponding levels for (a) 100 Hz, (b) 200 Hz, and (c) 500 Hz at MIL engine condition. The dashed box indicates the spatial region with source levels within 12 dB of the maximum at each frequency.

of a highly self-coherent source with salient features that can be described using relatively few independent sources. Even though the extent of the source distribution, as defined by the 12 dB down lines, range about 15, 12, and 9 m for each respective frequency, at 200 and 500 Hz, the coherence decays more quickly across the source than at 100 Hz. Because low coherence across a source distribution is indicative of multiple independent sources, multiple incoherent or partially coherent sources are required in a source model to produce source properties consistent with the results shown here, particularly above 200 Hz.

To more readily quantify source coherence properties across a wide frequency range, a coherence length, L_{γ^2}, is defined. The source L_{γ^2} is the smallest spatial distance, measured for each reference location, to a point where coherence drops below 0.5 and provides a convenient way to express coherence properties over a range of frequencies and spatial reference locations. The coherence lengths are displayed in Fig. 7 for reference locations within the top 12 dB of the frequency-dependent HM source levels, shown by the dashed line. The source coherence lengths vary significantly as a function of frequency, particularly for frequencies below 200 Hz. In addition, some frequencies exhibit spatial variation in L_{γ^2} across the source extent. For example, the L_{γ^2} values between 70 and 200 Hz increase around $z = 13$ m before decreasing farther downstream. The location of this peak in L_{γ^2} is about 4 m farther downstream than the maximum source level locations for frequencies below 125 Hz in Fig. 3, and even farther away from the respective maxima for frequencies above 125 Hz. This local peak in L_{γ^2} may indicate a source that is spatially separated from other sources that are present in the maximum source level region, as the increased L_{γ^2} values generally do not extend past the maximum source level locations.

A comparison of the source extents and coherence lengths provide insights into the nature of the sources. For example, a single distributed, coherent source has L_{γ^2} values at least as large as the source size, in the absence of noise. If multiple independent, distributed sources are present and overlapping, the L_{γ^2} values decrease according to the relative source strengths. Thus, the limited L_{γ^2} values within the source region in Fig. 7 signify that multiple uncorrelated or partially correlated sources comprise the jet noise source. Knowledge of the spatiospectral variation in L_{γ^2} across the source extent provides increased understanding nature of the jet noise sources and is useful in designing ESMs to more accurately model these features.

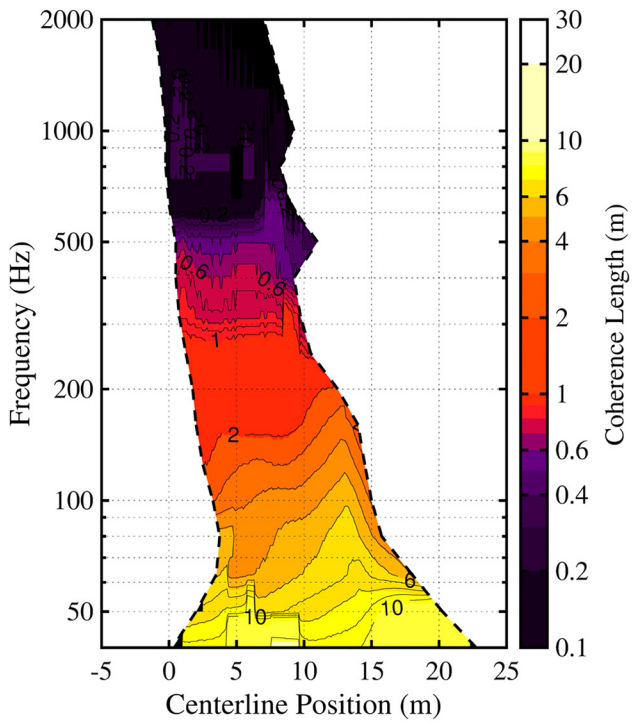

FIG. 7. (Color online) Source L_{γ^2} values calculated from the SCSM, for locations with source strength densities within 12 dB of the maximum at each frequency, obtained from UPAINT-HM applied to the full ground array at MIL engine condition.

E. Subarray beamforming analysis

The prior results utilized the entire measurement aperture (30 m) as input to the HM to find a corresponding ESM. Because there is high variability in the jet noise field, including regions dominated by mixing-noise radiation,[16,60,63] a decomposition of the noise using subarrays may yield unique source properties and insights in terms of acoustic source levels and coherence lengths. In one full-scale measurement example, Neilsen *et al.*[40] characterized tactical jet mixing noise using fine- and large-scale similarity (FSS and LSS) spectra derived using the two-source theory of jet mixing noise. They found that at MIL engine condition, FSS spectra represent the dominant radiation features for directivities up to about 100° ($z = 7.5$ m) and LSS spectra represent the dominant radiation levels farther downstream. Building upon these distinctions, the goal of this section is to characterize the differences in equivalent sources associated with the regions assigned to large- and fine-scale radiation, both in terms of levels and source coherence properties.

The measurement array is subdivided into two parts, consisting of the first 20 elements to the sideline of the jet ($-3.0\,\text{m} < z < 8.5\,\text{m}$) and the remaining 30 elements located farther downstream ($9.1\,\text{m} < z < 27.7\,\text{m}$). The $z = 8.5$ m division point roughly corresponds to the location of lowest L_{γ^2} of the sound field measured along the array at INT and AB, as shown in Fig. 12 in Ref. 29. The low field L_{γ^2} values at this point indicate a possible transition point between the dominant radiation of two or more independent sources of similar strength, confirming the transition region found by Neilsen *et al.*[40] where the measured spectral shapes change from agreeing with the FSS spectra to that of the LSS.

The complex spectra from each subarray are input separately to the UPAINT-HM method to estimate the source properties, and the resulting frequency-dependent source levels, $\mathbf{q}_{\text{U-HM}}$, are displayed in Fig. 8. The HM results of the sideline subarray ($z \leq 8.5$ m) in Fig. 8(a) show a source that remains nearly stationary, with the maximum source location moving from 2.8 m at 100 Hz to 2.0 m at 800 Hz. The source extent gradually contracts in size with increasing frequency from about 6.1 m at 100 Hz to about 3.3 m at 800 Hz, as measured using the contours 3 dB down from the peak level. In contrast, the maximum source location using the downstream subarray measurements in Fig. 8(b) varies much more with frequency (8.5 m at 100 Hz to 4.9 m at 800 Hz), while the source extent remains nearly constant [although the source extent may be slightly enlarged due to the UPAINT processing above 280 Hz (see Sec. III B)]. In addition, the source extent and peak location undergoes a sharp transition at 100–200 Hz similar to the one seen in Fig. 3 where the extent contracts by 1.2 m and the peak level location shifts upstream by 3.3 m. A grating lobe also exists at 500 Hz, around $z = 20$ m, which was not entirely removed in the UPAINT process and which slightly modifies the results.

Comparisons with spectral and intensity analyses performed on the same dataset provide insight into the differences in the subarray results. Neilsen *et al.*[40] showed that while the fine-scale spectral radiation levels are highest between 500 and 3000 Hz and do not strongly vary as a function of radiation

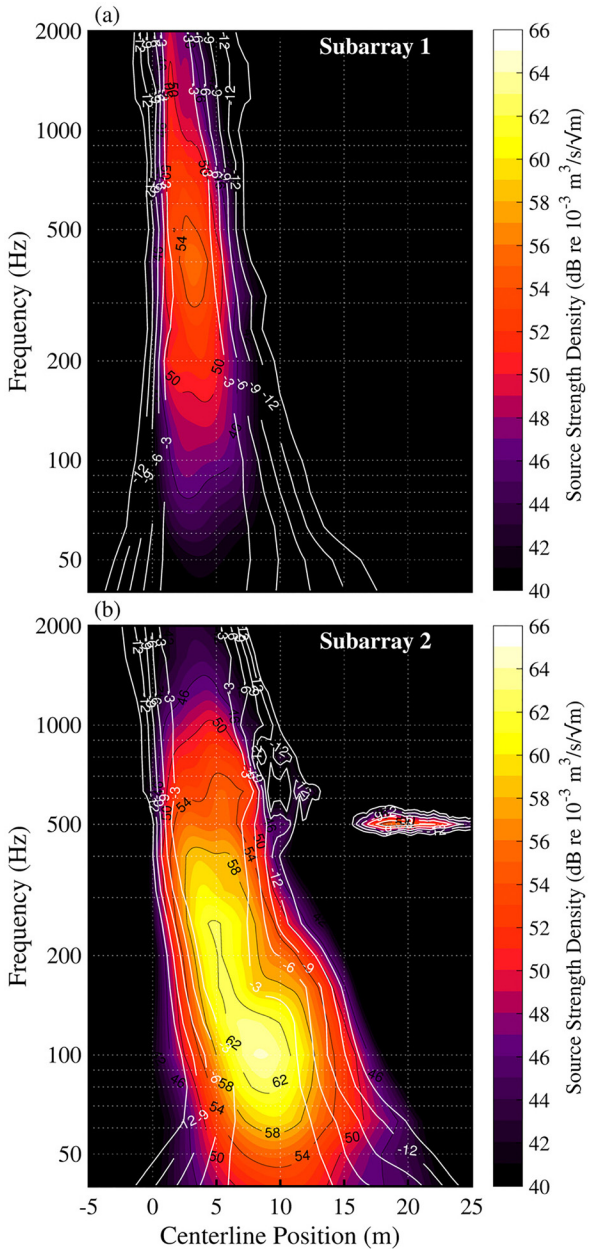

FIG. 8. (Color online) Source strength density, $q_{\text{U-HM}}$, using subarrays of (a) microphones $1-20$ [$z \leq 8.5$ m; sideline] and (b) microphones 21–50 [$z > 8.5$ m; downstream] using ground-array measurements of tactical aircraft noise at MIL engine condition. Similar to Fig. 3(b).

angle, the large-scale similarity spectral levels peak in value between 100–500 Hz and are most prominent at directivities of 110°–140° ($z = 10$–20 m along the measurement array). These trends are confirmed by the dominance of the downstream-subarray source levels for frequencies below 500 Hz [Fig. 8(b)] and the relatively larger role of the sideline-subarray source above 500 Hz [Fig. 8(a)]. This trend is also observed by Stout *et al.*[63] who used acoustic vector intensity measurements to show that above 500 Hz the angular span of the peak acoustic intensity vectors increases significantly, i.e., the sound radiation is more omnidirectional. This change to a more omnidirectional source as frequency increases can be explained by the relative amplitude gain of the sideline subarray source strengths with respect to the downstream subarray source strengths.

Using the SCSM from HM applied to the two subarrays, the source L_{γ^2} values are calculated from the source coherence (as in Fig. 7). The sideline-derived L_{γ^2} in Fig. 9(a) are about 2 m at 100 Hz, about 1 m at 200 Hz, and much less than 1 m at 500 Hz. The downstream-derived L_{γ^2} in Fig. 9(b) are generally more than double those from the sideline subarray [Fig. 9(a)] at a given frequency. The differences of the L_{γ^2} values collected from the arrays are even more pronounced below 100 Hz. These results show that the L_{γ^2} are low for the sideline-subarray source estimates, even for frequencies below 100 Hz, relative to the downstream-subarray source L_{γ^2} values.

The source coherence analysis provides insights into the differences of the subarray source estimates beyond the level-based findings. The relatively low source L_{γ^2} values from the sideline-based source relative to those from the downstream-based source indicate that the downstream-radiating sources are much more spatially distributed and correlated compared to the sideline radiation. The source level and coherence results suggest that the sideline subarray characterizes more omnidirectional, less coherent sources whereas the downstream subarray extracted source is comprised of more distributed and correlated sources with radiation directive towards high aft angles, in support of a two-source jet noise model interpretation.[16]

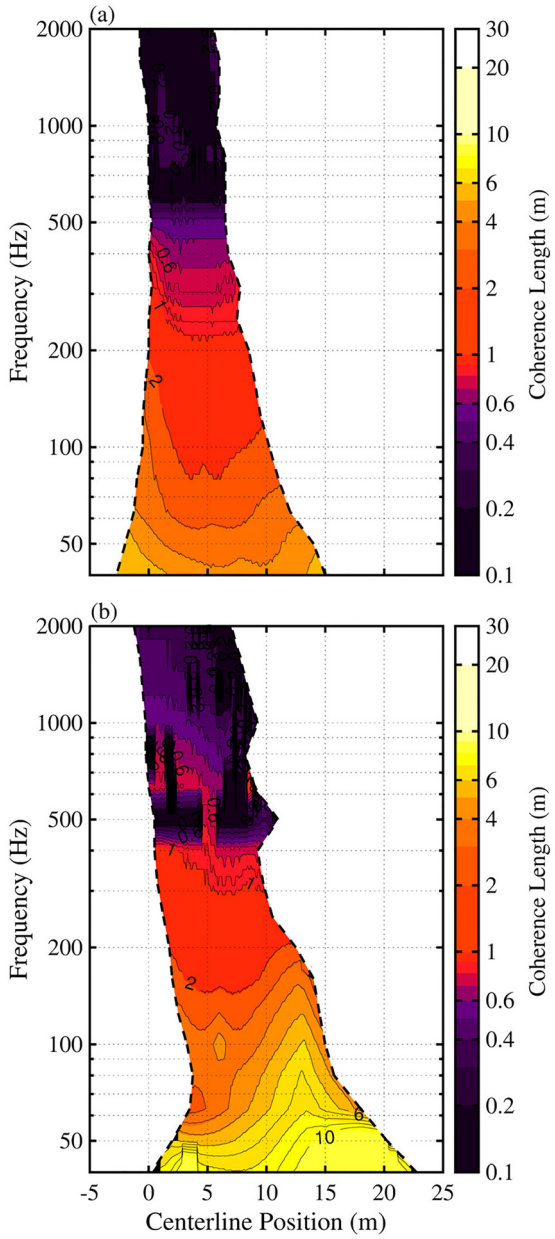

FIG. 9. (Color online) Source L_{γ^2} values calculated from the SCSM obtained from UPAINT-HM applied to subarrays of (a) microphones $1-20$ [$z \leq 8.5$ m; sideline] and (b) microphones $21-50$ [$z > 8.5$ m; downstream] at MIL engine condition. Similar to Fig. 7.

F. Engine condition analysis

The preceding analyses were for the military aircraft engine operating MIL power. In this section, the HM is applied to the full ground array for two additional engine conditions, namely, intermediate (INTER) and afterburner (AB; 150% ETR), to understand the engine-specific source level and coherence characteristics. The source estimates are calculated for INTER and AB engine conditions using UPAINT-HM, and the resulting source strength densities, $\mathbf{q}_{\mathrm{U-HM}}$, are shown in Fig. 10. At INTER, the source distribution is closer to the origin and the extent is smaller as compared to the MIL HM source estimates in Fig. 3(b). The maximum source levels at INTER occur between 100 and 200 Hz, and although there is a large shift in the peak location in this region, the dip in level between the two frequencies is not obvious. In contrast, the frequency-dependent source extents at AB condition are generally larger and located farther downstream of the nozzle exit. Two distinct maxima appear in the source strengths, and a transition region around 200 Hz is evident. The trends support the analysis by Stout *et al.*,[63] who estimated the source distribution location using ray-traces of vector intensity measurements and found that the AB source distribution was located about 1 m farther downstream and was 1 m smaller in extent than the MIL source distribution. They also observed a transition region at about 200 Hz where the maximum source region shifted upstream by 3–4 m from 100 to 300 Hz in both engine cases.

In addition to the intensity analysis results of Stout *et al.*, Wall *et al.*[55] used multisource, statistically optimized near-field acoustical holography (M-SONAH) to estimate the pressure levels at the source distribution for INTER, MIL, and AB conditions. A comparison of the UPAINT-HM method and M-SONAH results is shown in Table I. The holography results used nonsynchronous measurements in a patch-and-scan technique at the scan line, stitched together into partial fields using ground array measurements as a reference.[21,65] This provided a 153 element array with 0.30 m interelement spacing. The HM results used the 50-element ground array measurements, with 0.61 m interelement spacing, as input. Because the holography results were given as pressure estimates along the engine nozzle lip line (~0.3 m from the jet centerline), a Rayleigh integration of the HM results was performed to predict the lip-line pressures. The peak location and extent of the top 3 dB of the estimated pressure distributions are provided for each engine condition. Both methods generally show that the peak location

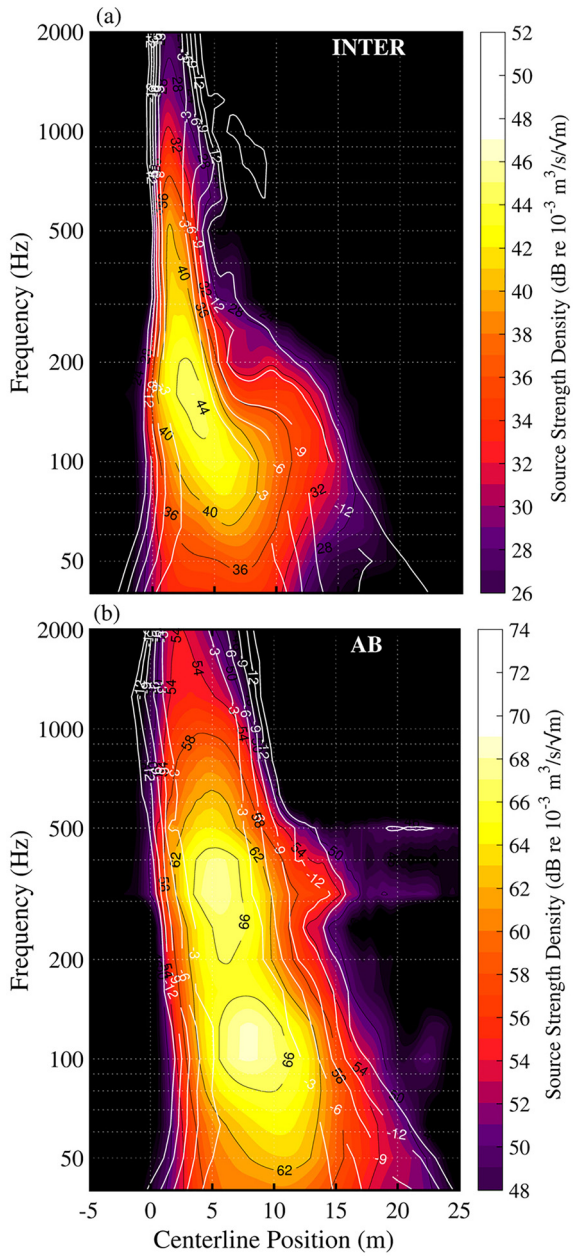

FIG. 10. (Color online) Source strength density, q_{U-HM}, using the full ground array at (a) INTER and (b) AB engine conditions. Similar to Fig. 3(b).

TABLE I. Comparison of source estimates between engine conditions for the peak location and spatial aperture (width) over which the pressure distributions along the nozzle lip line from UPAINT-HM and the M-SONAH output (from Ref. 55) is within 3 dB of the maximum. Results are in meters.

	100 Hz		200 Hz		500 Hz	
Engine condition	Peak	3 dB Width	Peak	3 dB Width	Peak	3 dB Width
UPAINT-HM						
INTER	6.4	7.0	3.1	3.6	1.9	2.0
MIL (100% ETR)	8.7	7.0	5.4	4.1	3.9	5.1
AB (150% ETR)	8.7	6.3	6.5	5.8	4.7	5.9
M-SONAH						
INTER	2.5	>5.5	2.0	3.0	1.5	>2.2
MIL (100% ETR)	7.3	7.4	5.0	4.9	3.0	4.0
AB (150% ETR)	8.2	8.2	6.0	5.8	4.9	5.0

moves downstream and the source extent enlarges with increasing engine condition. The peak locations and source level distributions of the two methods are within 1.0 m for the three frequencies shown, apart from the peak level location at INTER at 100 Hz where the results deviate by nearly 4 m. However, the holography results in this case show higher variation of the peak level location (e.g., below 100 Hz), suggesting that the source distribution levels near the peak location roll off more gently at these frequencies. In addition, the holography reconstructions were truncated according to the uncertainty, particularly for the INTER condition, and a lower bound on the width is given.

Additional analyses of the HM results as a function of engine conditions are provided in Fig. 11, where the L_{γ^2} values are shown for the INTER and AB conditions. In Fig. 11(a), the INTER L_{γ^2} values below 200 Hz show more

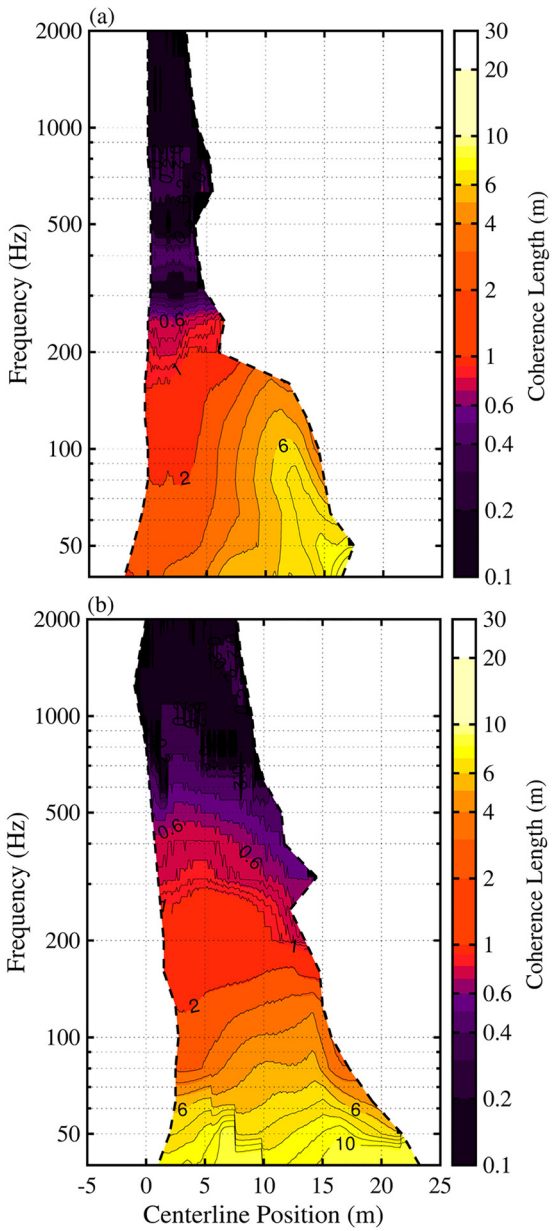

FIG. 11. (Color online) Source L_{γ^2} values for (a) INTER and (b) AB engine conditions from the SCSM obtained from UPAINT-HM applied to the full ground array. Similar to Fig. 7.

variation as a function of reference position compared to those of MIL in Fig. 7 or AB in Fig. 11(b), including a dip in the L_{γ^2} results to <2 m at 100 Hz and about $z = 3$ m. The L_{γ^2} values at INTER farther downstream are much higher, with values approaching 6 m at 100 Hz. At AB, the L_{γ^2} results show less variation as a function of reference position. Interestingly, the AB L_{γ^2} values are generally less than those at MIL. Furthermore, the INTER L_{γ^2} values are slightly larger than those at MIL for centerline positions of $z > 10$ m, although the opposite is true for $z < 10$ m. While the low L_{γ^2} values at INTER for $z < 10$ m is likely due to the stronger relative contribution of FSS related noise, the high L_{γ^2} values for both INTER and MIL conditions at $z = 12$–13 m suggest a similar mechanism that is responsible for the large values. Finally, L_{γ^2} values greater than 8 m are present in the MIL (and AB) results between 50–60 Hz regardless of the reference location. The large L_{γ^2} below 60 Hz at both MIL and AB suggest that a primary, distributed source radiates at levels well above any additional potential contributors at this frequency.

IV. CONCLUSION

Phased-array methods have been successfully applied to measurements of full-scale tactical aircraft engine noise at multiple operating conditions using a mid-field, linear measurement array. The HM was selected from results of a numerical study of a distributed-source model performed in Ref. 35; the robust nature of the HM produced source estimates that varied smoothly with frequency. In addition, the unwrapped-phase array interpolation (UPAINT) method has been added to the HM processing to increase the bandwidth of the results. The UPAINT algorithm interpolates across the measurement levels and phase values to artificially increase the perceived array measurement density and, thus, remove negative effects caused by grating lobes. When applied in conjunction with the HM, the frequency bandwidth of reasonable source level estimates has been extended to approximately seven times the array spatial Nyquist frequency, by significantly reducing the adverse effects of grating lobes.

The HM source distribution at military engine condition (MIL) has been used to estimate the source self-coherence. At 100 Hz, the source has been shown to be highly self-coherent, while at 200 and 500 Hz, the source coherence confirms that multiple independent sources are required to adequately model the source at this frequency. These results have been shown in terms of coherence lengths (L_{γ^2}) to more efficiently represent the data. The phase speed has also been estimated using the HM-based source estimates, which can be used to determine the primary directivity of the source, and results corroborate similar acoustic vector intensity-based studies.[63]

In addition, the jet noise source has been further investigated by applying UPAINT-HM separately to two subarrays selected to separate the sideline radiation from radiation located farther downstream. The source estimated using the sideline subarray is centered at about 2.5 m and does not significantly vary with increasing frequency. However, the source estimated using the downstream subarray varies significantly in location and extent with frequency, and accounts for most of the overall source levels obtained using the full array. The HM-based source levels from the sideline subarray peak at about 500 Hz, and the relative amplitude of this source increases with respect to that of the downstream subarray as frequency increases. These findings suggest that the source estimated by the upstream subarray characterizes an omnidirectional-type source whereas the downstream subarray source is much more directive towards high radiation angles. In addition, an analysis of the coherence properties resulting from the two subarrays has revealed that the downstream-based source coherence lengths are approximately double the values of the sideline-derived source for a given frequency. The level and coherence results point to omnidirectional sideline radiation, which is derived of multiple independent sources. In contrast, the downstream radiation is much more directed and generated with higher amplitude sources that are more self-coherent. These findings are consistent with a two-source jet noise model.[16]

Finally, source estimates have been calculated along the jet centerline for three engine conditions ranging from intermediate (INTER) to full afterburner (AB). The source extent and peak level locations were compared with source characterizations using near-field acoustical holography and vector intensity methods. A comparison of the nozzle lip line pressure estimates from the UPAINT-HM results and the holography reconstructions has shown that the estimated peak source locations and extents were mostly within 1 m for the frequency cases tested at all engine conditions. A coherence analysis has revealed that the coherence lengths at AB are generally less than those at MIL for a given frequency as well as for INTER towards the jet nozzle. Thus, additional partially correlated sources are required to adequately model higher engine conditions. However, the INTER and MIL L_{γ^2} values were distinctly higher for distances greater than 12 m from the nozzle. This finding indicates the preeminence of a source distribution in this region that exists for both engine conditions.

This work has developed a one-dimensional, source characterization of a full-scale jet noise source. The UPAINT-HM results have provided a complex source cross spectral matrix that, when considered as an equivalent source model, constitute a full-order model. However, an analytical reduced-order model of the HM results could similarly be used that could provide a more physically intuitive framework. For example, axial wavepackets have been used to represent the turbulent, hydrodynamic, and acoustic jet noise properties and provide a suitable model to decompose the HM results.[3] Further phased-array work to characterize the azimuthal variation of the source is expected to provide additional insights to the source self-coherence as well as the azimuthal variation as engine condition and frequency vary. These efforts will provide better understanding of the source characteristics of tactical jet noise, thus allowing for improved models to predict the radiation.

ACKNOWLEDGMENTS

The authors gratefully acknowledge the funding for this analysis from the Office of Naval Research (Grant No.

N000141410494). The measurements were funded by the U.S. Air Force Research Laboratory (USAFRL) through the Small Business Innovation Research program, and supported through a cooperative research and development agreement between Blue Ridge Research and Consulting, Brigham Young University, and the U.S. Air Force. This research was supported in part by the appointment of B.M.H. to the Student Research Participation Program at USAFRL, 711th Human Performance Wing, Human Effectiveness Directorate, Warfighter Interface Branch, Battlespace Acoustics Branch administered by the Oak Ridge Institute for Science and Education through an interagency agreement between the U.S. Department of Energy and USAFRL. DISTRIBUTION STATEMENT A. Approved for public release: distribution is unlimited. 88ABW Cleared 03/19/18; 88ABW-2018-1357.

[1]Y. Khalighi, J. W. Nichols, S. Lele, F. Ham, and P. Moin, "Unstructured large eddy simulation for prediction of noise issued from turbulent jets in various configurations," AIAA Paper 2011-2886 (2011).
[2]T. Suzuki, "A review of diagnostic studies on jet-noise sources and generation mechanisms of subsonically convecting jets," Fluid Dyn. Res. **42**, 014001 (2010).
[3]P. Jordan and T. Colonius, "Wave packets and turbulent jet noise," Annu. Rev. Fluid Mech. **45**, 173–195 (2013).
[4]A. Towne, T. Colonius, P. Jordan, A. V. Cavalieri, and G. A. Brès, "Stochastic and nonlinear forcing of wavepackets in a Mach 0.9 jet," AIAA Paper 2015-2217 (2015).
[5]Q. Leclère, A. Pereira, C. Bailly, J. Antoni, and C. Picard, "A unified formalism for acoustic imaging based on microphone array measurements," Int. J. Aeroacoust. **16**, 431–456 (2017).
[6]R. Merino-Martínez, P. Sijtsma, M. Snellen, T. Ahlefeldt, J. Antoni, C. J. Bahr, D. Blacodon, D. Ernst, A. Finez, S. Funke, T. F. Geyer, S. Haxter, G. Herold, X. Huang, W. M. Humphreys, Q. Leclère, A. Malgoezar, U. Michel, T. Padois, A. Pereira, C. Picard, E. Sarradj, H. Siller, D. G. Simons, and C. Spehr, "A review of acoustic imaging methods using phased microphone arrays," CEAS Aeronaut. J. **10**, 197–230 (2019).
[7]S. R. Venkatesh, D. R. Polak, and S. Narayanan, "Beamforming algorithm for distributed source localization and its application to jet noise," AIAA J. **41**, 1238–1246 (2003).
[8]S. S. Lee and J. Bridges, "Phased-array measurements of single flow hot jets," AIAA Paper 2005-2842 (2005).
[9]R. Schlinker, S. Liljenberg, D. Polak, K. Post, C. Chipman, and A. Stern, "Supersonic jet noise source characteristics and propagation: Engine and model scale," AIAA Paper 2007-3623 (2007).
[10]L. Brusniak, J. Underbrink, E. Nesbitt, D. Lynch, and M. Martinez, "Phased array measurements of full-scale engine exhaust noise," AIAA Paper 2007-3612 (2007).
[11]R. Dougherty and J. Mendoza, "Phased array beamforming with 100-foot polar arc microphones in a static engine noise test," AIAA Paper 2008-51 (2008).
[12]C. K. W. Tam, "Jet noise: Since 1952," Theor. Comp. Fluid Dyn. **10**, 393–405 (1998).
[13]K. Viswanathan, M. Alkislar, and M. Czech, "Characteristics of the shock noise component of jet noise," AIAA J. **48**, 25–46 (2010).
[14]S. S. Lee and J. Bridges, "Phased-array study of dual-flow jet noise: Effect of nozzles and mixers," AIAA Paper 2006-2647 (2006).
[15]T. F. Brooks and W. M. Humphreys, Jr., "Extension of DAMAS phased array processing for spatial coherence determination (DAMAS-C)," AIAA Paper 2006-2654 (2006).
[16]C. K. W. Tam, K. Viswanathan, K. K. Ahuja, and J. Panda, "The sources of jet noise: Experimental evidence," J. Fluid Mech. **615**, 253–292 (2008).
[17]R. P. Dougherty, "Improved generalized inverse beamforming for jet noise," Int. J. Aeroacoust. **11**, 259–290 (2012).
[18]T. Padois, P.-A. Gauthier, and A. Berry, "Inverse problem with beamforming regularization matrix applied to sound source localization in closed wind-tunnel using microphone array," J. Sound Vib. **333**, 6858–6868 (2014).
[19]T. F. Brooks, W. M. Humphreys, and G. E. Plassman, "DAMAS processing for a phased array study in the NASA Langley Jet Noise Laboratory," AIAA Paper 2010-3780 (2010).
[20]J. Hald, "Combined NAH and beamforming using the same microphone array," Sound Vib. **38**, 18–27 (2004), available at http://www.sandv.com/downloads/0412hald.pdf.
[21]A. T. Wall, K. L. Gee, M. M. James, K. A. Bradley, S. A. McInerny, and T. B. Neilsen, "Near-field noise measurements of a high-performance military jet aircraft," Noise Control Eng. J. **60**, 421–434 (2012).
[22]U. Michel and S. Funke, "Noise source analysis of an aeroengine with a new inverse method SODIX," AIAA Paper 2008-2860 (2008).
[23]E. G. Williams, "Regularization methods for near-field acoustical holography," J. Acoust. Soc. Am. **110**, 1976–1988 (2001).
[24]Z. Wang and S. F. Wu, "Helmholtz equation–least-squares method for reconstructing the acoustic pressure field," J. Acoust. Soc. Am. **102**, 2020–2032 (1997).
[25]T. F. Brooks and W. M. Humphreys, "A deconvolution approach for the mapping of acoustic sources (DAMAS) determined from phased microphone arrays," J. Sound Vib. **294**, 856–879 (2006).
[26]P. Sijtsma, "CLEAN based on spatial source coherence," Int. J. Aeroacoust.**6**, 357–374 (2007).
[27]V. Fleury and R. Davy, "Large-scale jet noise testing, reduction and methods validation 'EXEJET': 5. Analysis of jet-airfoil interaction noise by microphone array techniques," AIAA Paper 2014-3036 (2014).
[28]T. Padois, A. Berry, P.-A. Gauthier, and N. Joshi, "Beamforming matrix regularization and inverse problem for sound source localization: Application to aero-engine noise," AIAA Paper 2013-2212 (2013).
[29]B. M. Harker, T. B. Neilsen, K. L. Gee, A. T. Wall, and M. M. James, "Spatiotemporal correlation analysis of jet noise from a high-performance military aircraft," AIAA J. **54**, 1554–1566 (2016).
[30]C. K. Tam and S. Parrish, "Noise of high-performance aircrafts at afterburner," AIAA Paper 2014-2754 (2014).
[31]J. Liu, A. T. Corrigan, K. Kailasanath, and E. J. Gutmark, "Effects of temperature on noise generation in supersonic jets," AIAA Paper 2016-2937 (2016).
[32]A. T. Wall, K. L. Gee, T. B. Neilsen, B. M. Harker, S. A. McInerny, R. C. McKinley, and M. M. James, "Investigation of multi-lobed fighter jet noise sources using acoustical holography and partial field decomposition methods," AIAA Paper 2015-2379 (2015).
[33]T. Suzuki, "L1 generalized inverse beam-forming algorithm resolving coherent/incoherent, distributed and multipole sources," J. Sound Vib. **330**, 5835–5851 (2011).
[34]T. Yardibi, J. Li, P. Stoica, N. S. Zawodny, and L. N. Cattafesta, "A covariance fitting approach for correlated acoustic source mapping," J. Acoust. Soc. Am. **127**, 2920–2931 (2010).
[35]B. M. Harker, "Characterization of military aircraft jet noise using wavepacket analysis and other array processing methods," Ph.D.dissertation, Brigham Young University, Provo, UT, 2017.
[36]C. B. Goates, B. M. Harker, T. B. Neilsen, and K. L. Gee, "Extending the bandwidth of an acoustic beamforming array using phase unwrapping and array interpolation," J. Acoust. Soc. Am. **141**, EL407–EL412 (2017).
[37]K. L. Gee, M. Akamine, K. Okamoto, T. B. Neilsen, M. R. Cook, S. Tsutsumi, S. Teramoto, and T. Okunuki, "Characterization of supersonic laboratory-scale jet noise with vector acoustic intensity," AIAA Paper 2017-3519 (2017).
[38]V. Fleury, J. Bulté, and R. Davy, "Determination of acoustic directivity from microphone array measurements using correlated monopoles," AIAA Paper 2008-2855 (2008).
[39]Y. Du and P. J. Morris, "Numerical simulation of the effect of a low bypass cooling stream on supersonic jet noise," AIAA Paper 2014-1402 (2014).
[40]T. B. Neilsen, K. L. Gee, A. T. Wall, and M. M. James, "Similarity spectra analysis of high-performance jet aircraft noise," J. Acoust. Soc. Am. **133**, 2116–2125 (2013).
[41]T. Yardibi, J. Li, P. Stoica, and L. N. Cattafesta III, "Sparsity constrained deconvolution approaches for acoustic source mapping," J. Acoust. Soc. Am. **123**, 2631–2642 (2008).
[42]P. A. Ravetta, R. A. Burdisso, and W. F. Ng, "Noise source localization and optimization of phased-array results," AIAA J. **47**, 2520–2533 (2009).
[43]F. Presezniak, P. A. Zavala, G. Steenackers, K. Janssens, J. R. Arruda, W. Desmet, and P. Guillaume, "Acoustic source identification using a generalized weighted inverse beamforming technique," Mech. Syst. Signal Process. **32**, 349–358 (2012).

[44]P. Zavala, W. De Roeck, K. Janssens, J. Arruda, P. Sas, and W. Desmet, "Generalized inverse beamforming with optimized regularization strategy," Mech. Syst. Signal Process. **25**, 928–939 (2011).
[45]R. P. Dougherty, "Functional beamforming for aeroacoustic source distributions," AIAA Paper 2014-3066 (2014).
[46]T. K. Moon and W. C. Stirling, in *Mathematical Methods and Algorithms for Signal Processing* (Prentice Hall, Englewood Cliffs, NJ, 2000), 139 pp.
[47]D. N. Swingler and R. S. Walker, "Line-array beamforming using linear prediction for aperture interpolation and extrapolation," IEEE Trans. Acoust., Speech, Signal Process. **37**, 16–30 (1989).
[48]J. Antoni, "A Bayesian approach to sound source reconstruction: Optimal basis, regularization, and focusing," J. Acoust. Soc. Am. **131**, 2873–2890 (2012).
[49]M. R. Cook, K. L. Gee, S. D. Sommerfeldt, and T. B. Neilsen, "Coherence-based phase unwrapping for broadband signals," Proc. Meet. Acoust. **30**, 055005 (2017).
[50]S. Noschese and L. Reichel, "Inverse problems for regularization matrices," Numer. Algorithms **60**, 531–544 (2012).
[51]R. P. Dougherty, "Beamforming in acoustic testing," in *Experimental Fluid Mechanics Series* (Springer-Verlag GmbH, Berlin, Germany, 2002).
[52]K. L. Gee, J. M. Downing, M. M. James, R. C. McKinley, R. L. McKinley, T. B. Neilsen, and A. T. Wall, "Nonlinear evolution of noise from a military jet aircraft during ground run-up," AIAA Paper 2012-2258 (2012).
[53]C. K. W. Tam, A. C. Aubert, and J. T. Spyropoulos, "On the dominant noise components of tactical aircraft: Laboratory to full scale," AIAA Paper 2017-3516 (2017).
[54]A. T. Wall, K. M. Leete, K. L. Gee, T. B. Neilsen, M. M. James, and R. L. McKinley, "Preliminary investigation of multiple fighter jet noise sources using acoustical holography," AIAA Paper 2017-3520 (2017).
[55]A. T. Wall, K. L. Gee, T. B. Neilsen, R. L. McKinley, and M. M. James, "Military jet noise source imaging using multisource statistically optimized near-field acoustical holography," J. Acoust. Soc. Am. **139**, 1938–1950 (2016).
[56]S. H. Swift, K. L. Gee, T. B. Neilsen, A. T. Wall, J. M. Downing, and M. M. James, "Spatiotemporal correlation analysis of jet noise from a round-nozzle supersonic aircraft," AIAA Paper 2018-3938 (2018).
[57]B. J. Greska, "Supersonic jet noise and its reduction using microjet injection," Ph.D. dissertation, The Florida State University, Tallahassee, FL, 2005.
[58]J. M. Seiner, M. K. Ponton, B. J. Jansen, and N. T. Lagen, "The effects of temperature on supersonic jet noise emission," in *Proceedings of 14th DGLR/AIAA Aeroacoustics Conference*, May 1992, pp. 295–307.
[59]A. Krothapalli, L. Venkatakrishnan, and L. Lourenco, "Crackle: A dominant component of supersonic jet mixing noise," AIAA Paper 2000-2024 (2000).
[60]K. Viswanathan, J. R. Underbrink, and L. Brusniak, "Space-time correlation measurements in near fields of jets," AIAA J. **49**, 1577–1599 (2011).
[61]W. J. Baars, C. E. Tinney, N. E. Murray, B. J. Jansen, and P. Panickar, "The effect of heat on turbulent mixing noise in supersonic jets," AIAA Paper 2011-1029 (2011).
[62]W. J. Baars and C. E. Tinney, "Shock-structures in the acoustic field of a Mach 3 jet with crackle," J. Sound Vib. **333**, 2539–2553 (2014).
[63]T. A. Stout, K. L. Gee, T. B. Neilsen, A. T. Wall, and M. M. James, "Source characterization of full-scale jet noise using acoustic intensity," Noise Control Eng. J.**63**, 522–536 (2015).
[64]K. M. Leete, A. T. Wall, K. L. Gee, T. B. Neilsen, B. M. Harker, and M. M. James, "Azimuthal coherence of the sound field in the vicinity of a high performance military aircraft," Proc. Meet. Acoust. **29**, 045007 (2016).
[65]J. Hald, "STSF-a unique Technique for scan-based near-field acoustic holography without restriction on coherence," B & K Technical Review No. 1 (1989).